3-1-2003

Interfacial Mixing in a Highly Stratified Estuary: 1. Characteristics of Mixing

David J. Kay
Portland State University

David A. Jay
Portland State University

Citation Details

Kay, D. J., & Jay, D. A. (2003). Interfacial mixing in a highly stratified estuary. 1. Characteristics of mixing. Journal Of Geophysical Research, 108(C3), 17-1-15.

JOURNAL OF GEOPHYSICAL RESEARCH, VOL. 108, NO. C3, 3072, doi:10.1029/2000JC000252, 2003

Interfacial mixing in a highly stratified estuary
1. Characteristics of mixing

David J. Kay
Geophysics, University of Washington, Seattle, Washington, USA

David A. Jay
Department of Environmental Science and Engineering, Oregon Graduate Institute, Portland, Oregon, USA

Received 26 January 2000; revised 18 February 2002; accepted 4 April 2002; published 13 March 2003.

[1] This article is Part I of a set of papers addressing mixing in a highly stratified estuary. Measurements of interfacial turbulence were made in Columbia River estuary under conditions of moderate river flow and neap tides. A flux correlation method was used to determine buoyancy fluxes, and fits to theoretical velocity and temperature variance spectra were used to measure turbulent kinetic and potential energy dissipation rates. At the measurement site in the interior of the estuary, mixing along the top of the salt wedge is found to occur only on ebb, during periods when the internal Froude number is supercritical. The wedge cannot, therefore, be in a quasiequilibrium state, and vertical mixing plays a dominant role in its ebb retreat. The turbulent Froude number Fr_T, which represents the ratio of effects of shear and stratification on the mixing, was found to be close to $Fr_T \approx 1$ during mixing episodes. This suggests an interplay between shear and buoyancy effects that corresponds to a condition of maximum mixing efficiency Γ. Γ is measured using both direct calculations of the buoyancy and dissipation terms in the turbulent kinetic energy (TKE) balance (this estimate of Γ is referred to as Γ_0), and by estimating the buoyancy term B by its relationship to χ_T, the dissipation of temperature variance (this estimate of Γ is referred to as Γ_d). Averages over several mixing events give $\Gamma_0 \approx 0.22$ and $\Gamma_d \approx 0.36$. Sources of bias in these measurements result from (1) approximations to the full TKE and available potential energy (APE) balances, (2) empirical constants used in fits of measured spectra in inertial subranges, (3) frame motion, and (4) high-pass filtering. The sign of the biases suggest that $0.22 < \Gamma < 0.36$. Flood-ebb asymmetry in mixing also results in a time dependent force balance (discussed further by *Kay and Jay* [2003]). This asymmetry is analyzed using a new method to determine profiles of the momentum balance during ebb mixing events. *INDEX TERMS:* 4546 Oceanography: Physical: Nearshore processes; 4568 Oceanography: Physical: Turbulence, diffusion, and mixing processes; *KEYWORDS:* estuary, turbulence, mixing efficiency, energy balance

Citation: Kay, D. J., and D. A. Jay, Interfacial mixing in a highly stratified estuary, 1, Characteristics of mixing, *J. Geophys. Res.*, *108*(C3), 3072, doi:10.1029/2000JC000252, 2003.

1. Introduction

[2] Mixing in estuaries is a major factor affecting circulation, sediment transport, and the fate of pollutants. The large impact of human development on estuarine environments makes imperative an effort to understand these systems. Internal mixing in shallow water stratified tidal flows is central to the understanding of salt wedge dynamics, yet is very difficult to measure. Modeling difficulties arise because the averaging procedure involved in the development of the Reynolds equations for turbulent flow results in a unclosed set of equations. Many different turbulence closure schemes have been proposed for various types of flow. However, lack of measurements in the environments of interest make assessment of even simple closure schemes difficult. Mixing is often used as a parameter, adjusted by the modeler, to match model output with data. More direct measurements of turbulence in estuaries are necessary, both to test assumptions going into numerical models and to deepen understanding of the underlying mechanisms. This paper is the first of a set of two papers addressing mixing in highly stratified estuaries. The goal of this paper is to present and interpret mixing measurements made at the freshwater-saltwater interface in the Columbia River. These measurements are used to calculate mixing parameters commonly used in estuarine models. (See Table 1 for descriptions of parameters used in this paper.) The second paper presents a new approach, the "method of constrained differences," to determine the estuarine momentum and salt

0148-0227/03/2000JC000252$09.00

balances in the presence of mixing and the method is applied to the Columbia River estuary. The output of the model is used to examine the global mixing budget in the estuary and its significance in the transport of scalars.

[3] Parameterization of mixing in models of stratified estuarine systems is necessary, but direct measurements of turbulence in stratified estuarine flows are rare. The effects of mixing may sometimes be inferred from evolution of the velocity and salinity profiles [*Geyer*, 1985], but only if the effects of advection of the velocity and salinity fields can be ignored. Efforts have also been made to measure turbulence with acoustic Doppler profilers [*Lu and Lueck*, 1999; *Gargett*, 1994; *Stacey et al.*, 1999]. Profilers allow the measurements of the large scales of turbulence, from which dissipation rates can be inferred using scaling estimates. Microprofilers have also been deployed in estuarine environments [*Peters*, 1997]. These profilers resolve smaller turbulent scales, but strong currents often make their application difficult. We discuss here the use of an acoustic Doppler velocimeter (Sontek ADV) and conductivity/temperature/depth (CTD) sensor to measure dissipation rates and buoyancy fluxes in an energetic estuarine environment.

[4] Direct measurements of turbulent dissipation rates and buoyancy fluxes are used here to address the following questions: (1) How does the energy of interfacial mixing vary over the tidal cycle, and what are the implications for the modeling of highly stratified estuaries? (2) What is the character of the observed turbulence as determined by the turbulent Reynolds number Re_T and Froude number Fr_T? (3) What is the mixing efficiency of the observed turbulence? The answers to these questions have implications for modeling stratified estuarine systems, the choice of mixing parameters, and the relevance of other ocean measurements to estuarine environments.

Table 1. Definitions of Parameters Used in Paper

Symbol	Description
G	internal Froude number
$F_{u,l}$	upper lower layer Froude numbers
$U_{u,l}$	average upper lower layer velocities, m s^{-1}
$H_{u,l}$	upper lower layer thickness, m
R_f	flux Richardson number
R_{fc}	critical flux Richardson number
Ri_g	gradient Richardson number
P	turbulent production rate, W s^{-1}
ϵ	turbulent dissipation rate, W s^{-1}
B	turbulent buoyancy flux, W s^{-1}
$K_{\rho,m,S,T}$	eddy diffusivities of density, momentum, salt, temperature, m^2 s^{-1}
Γ	mixing coefficient
Γ_0	mixing coefficient as determined by taking ratio B/ϵ
Γ_d	mixing coefficient as determined using dissipation method
χ_{pe}	potential energy dissipation rate, W s^{-1}
χ_T	temperature variance dissipation rate, °C s^{-1}
R_ρ	stability ratio
α_T	thermal expansion coefficient for water, $°C^{-1}$
β_S	haline contraction coefficient for water, ppt^{-1}
L_R, L_T, L_K	Ozmidov, Ellison, Kolmogorov scales, m
T_B, T_E	buoyancy period, eddy overturn timescale, s
Fr_T	turbulent Froude number
L_K	turbulent Reynolds number
E_k	turbulent energy density
$\phi_w(k_u)$	one-dimensional vertical velocity spectrum (as function of horizontal wavenumber)
$\phi_s(k_u)$	one-dimensional scalar spectrum (as function of horizontal wavenumber)

2. Background

2.1. Mixing and Salt Wedge Models

[5] The simplest models of salt wedge systems treat the tidal flow as a small correction to a steady-state residual (nontidal) problem [*Rattray and Mitsuda*, 1974; *Pedersen*, 1996; *Zhu*, 1996; *Jirka and Arita*, 1987]. The solution is sought for an arrested wedge in equilibrium under tidal mean current and density conditions. This approach assumes a two-layer flow with no salt exchange at the interface, and small velocities in the lower layer. Necessary conditions for equilibrium are (1) subcritical internal Froude number along the wedge, and (2) weak mixing. The internal Froude number, G, is defined as

$$G^2 = F_u^2 + F_l^2 = \frac{U_u^2}{g' H_u} + \frac{U_l^2}{g' H_l}, \tag{1}$$

where; F_u and F_l are the upper and lower layer Froude numbers, $g' = g\delta\rho/\rho_0$ is reduced gravity, U_u and U_l are the average upper and lower layer velocities, and H_u and H_l are the upper and lower layer thicknesses, respectively. When G becomes supercritical ($G > 1$), internal waves cannot travel upstream and amplification and instability may result. The arrested wedge theory requires that the internal Froude number become supercritical only at the mouth where the upper layer vanishes. If $G < 1$ along the wedge, time dependence effects can be superimposed on the equilibrium solution as long as the timescale associated with changes in barotropic flow are large compared with the time needed for internal waves to travel the length of the wedge. If these condition are not satisfied, the quasiequilibrium picture breaks down, complicating the modeling problem and requiring accurate parameterization of mixing [*Helfrich*, 1995]. Results discussed below show that $G > 1$ applies throughout the wedge on ebb.

2.2. Mixing Efficiency

[6] Supercritical flow on ebb ($G > 1$) results in substantial diapycnal mixing, a violation of one of the assumptions of simple wedge theories. If mixing should be included in such models, how is it best parameterized? A useful approach to the parameterization of mixing relies on the theory, supported by laboratory studies and ocean measurements, that fully developed turbulence proceeds at a critical value, R_{fc}, of the flux Richardson number, $R_f = \frac{B}{P}$, where B and P are the buoyancy and production terms in the turbulent kinetic energy (TKE) balance. In two-dimensional flow, with mean (U,W) and turbulent fluctuations (u',w') of horizontal and vertical velocity, respectively, $R_f \equiv \frac{-g}{\rho_0}\overline{\rho' w'}/\overline{u' w'} U_z$, where the overbars represent time average over turbulent timescales and coordinate subscripts represent derivatives. In stably stratified flow, the flux Richardson number is the fraction of total TKE production that is lost to buoyancy, increasing the potential energy of water column. Thus, R_{fc} is an estimate of the effectiveness of the mixing in increasing the potential energy of the water column.

[7] Physical arguments suggest, furthermore, that R_f is significantly less than 1 in a steady flow. That is, production of turbulence by shear $\frac{\partial u}{\partial z}$ goes initially into u', and is

subsequently distributed by pressure-velocity correlations to v' and w'. Since there is viscous dissipation in each component, but buoyancy losses only in the vertical component, only a portion of the turbulent energy is utilized to increase the potential energy of the flow. Understanding the behavior of R_f, or equivalently the mixing efficiency, $\Gamma \equiv R_f/(1-R_f) \equiv \frac{B}{\epsilon}$, is very important as a guide to modeling efforts. Although R_f is key to turbulence parameterization, there have been very few estimates of R_f in high Reynolds number flows found in estuarine interfacial mixing [*Peters*, 1997].

2.3. Measurement of R_{fc} and Γ

[8] Accurate estimates of the Γ would allow the use of more easily measured mean and dissipation-scale quantities to estimate the turbulent diffusivities of momentum and salt. The standard approach used in the ocean begins from a simplified TKE balance of production (P), viscous dissipation (ϵ) and losses to buoyancy (B) [*Osborn*, 1980],

$$-\underbrace{\overline{u'w'}U_z}_{P} = \underbrace{\bar{\epsilon}}_{\epsilon} + \underbrace{\frac{g}{\rho_0}\overline{\rho'w'}}_{B}. \tag{2}$$

The viscous dissipation rate ϵ is the rate of loss of kinetic energy to heat through the action of molecular viscosity. This balance excludes as small the effects of diffusion and advection of TKE, unsteadiness, and pressure-work forces. Direct measurements of turbulent heat flux and dissipation rates seem to validate this assumption in the ocean. However, its validity in shallow water flows, where large spatial and temporal gradients can exist, is not known. Using equation (2) the eddy diffusivities of density and momentum are

$$K_\rho = \frac{g}{\rho_0}\frac{\overline{w'\rho'}}{N^2} \qquad K_m = \frac{\overline{u'w'}}{Uz}. \tag{3}$$

These may be written in terms of R_f and gradients of mean quantities,

$$K_\rho = \frac{R_f\epsilon}{(1-R_f)N^2} \qquad K_m = \frac{\epsilon}{(1-R_f)U_z^2}, \tag{4}$$

where $N^2 = -\frac{g}{\rho_0}\frac{\partial \rho}{\partial z}$. Use of equation (3) requires determination of R_f or, more directly, Γ.

[9] The quantity Γ can be estimated by two methods. The first is a measurement of B and ϵ, allowing direct calculation of Γ as $\frac{B}{\epsilon}$. The mixing efficiency calculated by this method will henceforth be referred to as Γ_0. The second approach to determine Γ, called the "dissipation method" (resulting in an estimate denoted here by Γ_d) uses the model of *Osborn and Cox* [1972]. The Osborn-Cox model assumes a steady-state potential energy balance. Because the potential energy dissipation rate χ_{pe} cannot be directly measured in a salt-stratified fluid, it is estimated from the temperature variance dissipation rate $\chi_T = 2\kappa_T\overline{T_z'^2}$ where κ_T is the molecular diffusivity of temperature. A linear equation of state is used and the assumption is made that the ratio of dissipation rates of salinity variance to temperature variance is equal to the ratio of their respective contributions to the mean density gradient (or equivalently, $K_S = K_T$). This assumption is supported in this experiment by the close correlation between salinity and temperature in the turbulence measurements, below. χ_{pe} can then be determined from [*Gregg*, 1987]

$$\frac{\rho_0}{g}\chi_{pe} = \overline{\rho'w'} = \frac{\rho_0\alpha_T\chi_T}{2Tz}(1-1/R_\rho) \tag{5}$$

where R_ρ is the stability ratio $R_\rho = \frac{\alpha_T T_z}{\beta_S S_z}$, and the subscript z refers to the vertical spatial derivative. The quantities α_T and β_S are the thermal expansion and haline contraction coefficients, respectively. The linear equation of state $N^2 = g\alpha_T T_z(1-1/R\rho)$ can then be substituted in equation (5) to yield

$$\Gamma_d = \frac{\chi_{pe}}{\epsilon} = \frac{\chi_T N^2}{2\epsilon T_z^2}. \tag{6}$$

Because microprofilers collect data while moving through the water, it is generally easier to measure small-scale fluctuations in density than in velocity. For this reason, the Cox model is most often used to determine mixing efficiency. Comparisons of the two methods have been made in tidal-front turbulence [*Gargett and Moum*, 1995] but not in estuaries. We make the first such comparison here.

2.4. Mixing Characteristics

[10] Stratification effects on turbulence are characterized by the dominant length and timescales associated with stable and unstable fluctuations. In neutrally or weakly stratified turbulent flow, the size of eddies is constrained by the distance to external boundaries, the bed or free surface. As stratification increases without increased turbulent production, the eddy size is limited by the increased energy needed to overturn larger eddies in the presence of the background density gradient. Limitation of the length scale of turbulence by stratification has profound effects on the ability of the flow to diffuse momentum, density, and suspended particulate matter.

[11] Three important length scales exist in a stratified turbulent shear flow. The buoyancy or Ozmidov scale $L_R = \left(\frac{\epsilon}{N^3}\right)^{1/2}$ is the upper limit of the vertical extent of turbulent overturns, i. e., the scale of overturns whose potential energy results from utilization of all of the turbulent kinetic energy (TKE) in the turbulence. Larger scales of turbulent motion are confined to horizontal motions [*Ozmidov*, 1965]. The typical vertical displacement of fluid, $L_T = \frac{-\rho'_{rms}}{\bar{\rho}_z}$, is the turbulence scale (also called the Ellison scale [*Ellison*, 1957]). The quantity ρ'_{rms} is the root mean squared variance of density as measured by a density sensor recording at a fixed position in the flow. The Kolmogorov scale, $L_K = \left(\frac{\nu^3}{\epsilon}\right)^{1/4}$, where ν is the kinematic viscosity, is the length scale at which the viscous effects become important (typically a fraction of a millimeter or less in estuarine mixing). A flow is found to be fully turbulent and isotropic at length scales L satisfying $C_1L_R > L > C_2L_K$ ($C_1 = O(1)$, $C_2 = O(10)$) and its fluctuations follow $k^{-5/3}$ spectral scaling [*Itsweire and Helland*, 1989]. Larger length scales $L > C_1L_R$ have insufficient energy to overturn and wave-like oscillations result [*Stillinger et al.*, 1983].

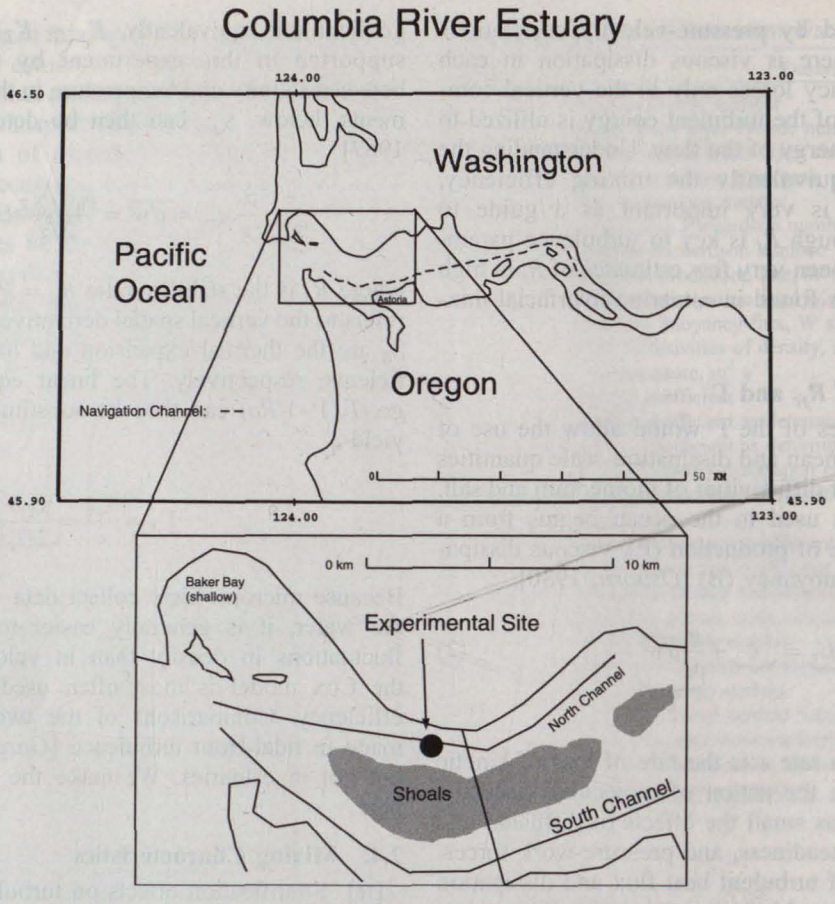

Figure 1. Location map of the Columbia River estuary. The two main channels of estuary are shown in the inset. Data collection took place in the north channel, historically the largest channel of the river. The north channel averages about 15–20 m in depth. The south channel has been developed for navigation.

[12] The nature of turbulence can be characterized by the turbulent Froude and Reynolds numbers expressed in terms of velocity and length scales [*Ivey and Imberger*, 1991; *Luketina and Imberger*, 1989],

$$Fr_T = \frac{q}{NL_T} = \frac{T_B}{T_E} \qquad Re_T = \frac{qL_T}{\nu} \tag{7}$$

where q is the scale of velocity fluctuations, T_B is the buoyancy period, and T_E is the eddy overturn time-scale. Under the assumption that the energy of eddies is dissipated in one overturn one can write $q = (\epsilon\ L_T)^{1/3}$, so that $Fr_T = \left(\frac{\epsilon}{N^3 L_T^2}\right)^{1/3}$. Noting that $N^2 L_T^2$ is the available potential energy (APE), Fr_T can be interpreted alternately as the one-third power of the ratio of the dissipation of TKE to the maximum rate of release of APE locked up in instantaneous instabilities in the density profile, or two-thirds power of the ratio of L_R to L_T; $Fr_T = \left(\frac{\epsilon}{N(APE)}\right)^{1/3} = \left(\frac{L_R}{L_T}\right)^{2/3}$. If $Fr_T > 1$, the turbulence is energetic with dissipation exceeding the APE in overturn events. Dissipation must be balanced by either local production or the importation of TKE. If $Fr_T < 1$, the dissipation is less than the APE, and potential energy in instabilities is likely converted into internal waves [*Ivey and Imberger*, 1991]. In decaying grid turbulence, Fr_T and Re_T are used to examine the evolution of a flow from a state consisting only of mean and turbulent kinetic energy (directly downstream of grid) to a combination of kinetic energy and wave-like oscillations as the turbulence decays under the influence of stratification. In a continuously forced stratified shear flow (e.g., an estuarine interfacial layer) Fr_T and Re_T reflect the current balance of turbulent and internal wave oscillations.

3. Methods

3.1. Experimental Site

[13] The Columbia River (Figure 1) is the second largest river in western North America with an annual average flow of $\approx$7500 $m^3\ s^{-1}$ and a drainage basin area of 660, 500 km^2. The Columbia has two principal subbasins [*Sherwood et al.*, 1990]; a coastal subbasin (10% of the area) supplies about 25% of the total basin runoff, and a large arid eastern subbasin (90% of the area) supplies about 75% of the total basin runoff.

[14] The Columbia River estuary is best characterized as highly stratified during neap tides or strong riverflow and weakly stratified to partially mixed during spring tides. Tidal-monthly changes in tidal forcing generate a distinct neap-spring transition. This transition has implications for the residual flow dynamics during periods of low to moderate riverflow, resulting in the occupation of two distinct flow and stratification regimes over the tidal month. The range of stratification conditions are the result primarily of tidal-monthly changes in turbulent mixing, which (if riverflow

is constant) result from changes in tidal forcing. Spring tides are characterized by increased mixing due to the higher energy of tidal forcing. Except under conditions of extreme river flow, both stratification and tidal variations in stratification are reduced on spring tide, reducing the baroclinic contribution to the residual circulation [*Jay and Smith*, 1990]. *Jay and Smith* [1990] observed that the Columbia River could be classified as weakly stratified during low-flow spring tides with the channel configuration pertaining in 1980–1981. However, the weakly stratified state is very dependent on strong vertical mixing because riverflow in this system would rapidly restratify the estuary if mixing were not maintained on flood tide. The reduced tidal forcing and distinct character of the mixing during neap tides results in a very different salinity structure. During neap tides, bottom boundary generated turbulence is insufficient to extend mixing into the upper part of the flow. Although the channel deepening in the 1980s has caused the system to be partially mixed on spring tides, the persistence of a sharp interface on flood is unique to neap tides. This two-layer system allows increased salinity intrusion relative to more weakly stratified spring tides.

[15] A 30-hour experiment was conducted under neap conditions in the central region of the Columbia River estuary from 1300 PST, July 11, 1997 to 1900 PST, July 12, 1997. The river flow for the month of July 1997 averaged 6000 m^3 s^{-1}, a moderate flow for the Colombia River but high for midsummer. Data were collected in the north channel where the tides and currents are approximately rectilinear and reversing. There was a sharp asymmetry between flood and ebb. Flood currents were strongest at middepth, while strong ebb currents occur near the free surface.

3.2. Instrumentation and Data Collection

[16] A combination of small- and large-scale (in both time and space) measurements of velocity and density were made in order to observe both interfacial mixing and the estuarine contest, the tidal current and density fields. This was achieved by using a two-pronged approach involving water column profiles of velocity and density and fixed-depth time series of turbulent fluctuations in velocity and density. A uniform sampling procedure was followed throughout the 30-hour interfacial mixing experiment. For about 15 min each half hour, time series measurements of velocity and density fluctuations were made at a fixed depth. Because the pycnocline moved us and down tidally, a depth was chosen for each half hour on the basis of the previous density profile. At half-hour intervals density profiles were collected. ADCP data were collected continuously, The final data set included turbulence measurements of velocity and density in the interface, and profiles of background density and velocity, as described in the next several paragraphs.

[17] Mean velocity profiles were recorded with a vessel-mounted RDI 1.2 MHz narrow-band ADCP. Profiles were collected at a rate of ≈3 Hz using 1-m bins, and then averaged over 5 min (≈900 profiles). The small ship velocity was removed using the bottom tracking capabilities of the ADCP. Direction and position information were obtained using a gyrocompass and GPS navigation read directly by the RDI software. ADCP measurements errors are discussed by *Jay and Musiak* [1994].

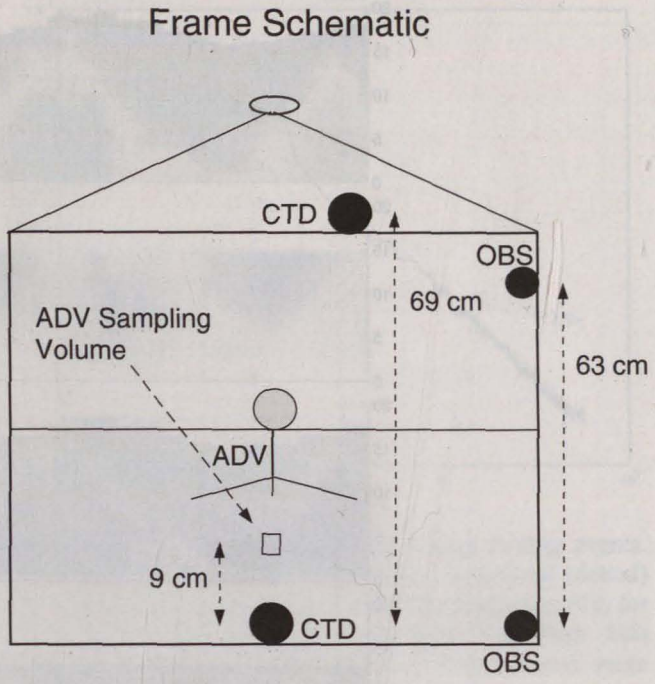

Figure 2. Schematic diagram of instrument frame. The frame was used for continuous collection of data at fixed depth in the interfacial region as well as for profiling. Instruments included two conductivity/temperature/depth (CTD) sensors, two optical backscatter turbidity sensors (OBS), and an acoustic Doppler velocimeter (ADV).

[18] Profiles of pressure, temperature, and conductivity were recorded using an Ocean Sensors OS-200 model conductivity/temperature/depth (CTD) profiler attached to the frame shown schematically in Figure 2. The OS-200 sampled temperature, pressure, conductivity, and OBS sensors at approximately 70 Hz. Averages of 10 CTD measurements were made internally to the CTD. These data were sent up a cable to a ship-board computer, given a time stamp, and recorded to disk at 7 Hz. CTD profile data were subsequently averaged with a triangular weighting into 0.20-m bins in the vertical. A typical CTD lowering speed was ≈0.3 m s^{-1}, resulting in averages of about 3–4 CTD measurements per profile data point.

[19] Measurements of turbulent velocity fluctuations were made with a field version of the Sontek downward-looking acoustic Doppler velocimeter (ADV). Advantages of the ADV for these measurements include unobstructed flow measurements, a rapid sampling rate of 25 Hz, and drift-free operation. The sensor consists of one 10-MHz transmitter situated at the center of a triangular array of three receiving transducers. The receivers are slanted 30° from the vertical axis through the transmitter. These three receivers focus on a sampling volume of $<(10^{-2}\ m)^3$, which is located 0.1 m from the transducers. The ADV operates by transmitting bursts of short acoustic pulses. A portion of the transmitted wave energy is reflected back toward the receiving transducers by particulates in the water. These transducers measure the return pulse during discrete "time windows" to collect only energy reflected from the focal sampling volume. The velocity of the water carrying the reflecting particles is proportional to the difference in phase measured

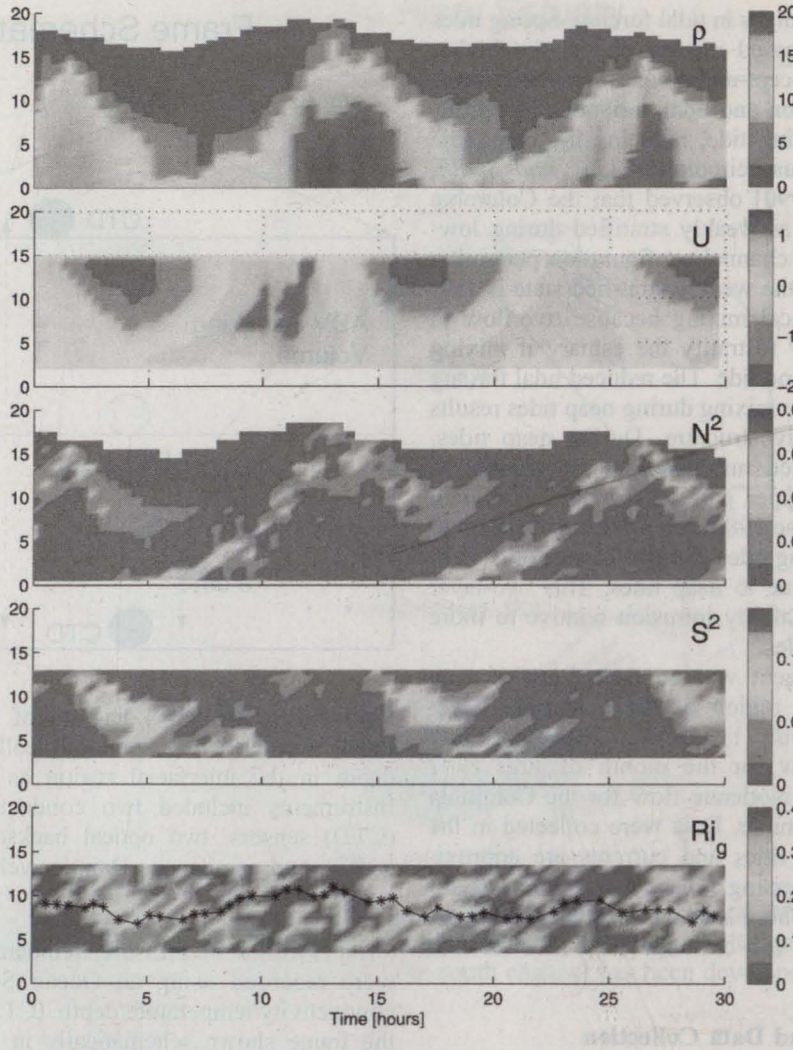

Figure 3. Contour fields of density, along-channel velocity, buoyancy frequency squared (N^2), shear squared (S^2), and Richardson number (Ri_g). All fields are shown relative to the start time of the data collection series, 1300 hours PST, July 11, 1997. Density profiles were collected with the CTD and velocity profiles were collected with the shipboard ADCP. Seaward velocities have a negative sign. See color version of this figure at back of this issue.

over successive pulses. A more detailed description of the operational principals of the ADV and similar pulse-to-pulse instruments is given by *Kraus et al.* [1994], *Lohrmann et al.* [1990], and *Lohrmann et al.* [1994].

4. Analysis and Results

4.1. Mean Velocity and Density Structure

[20] Figure 3 depicts the density and velocity fields during the experimental period. The density field (expressed as σ_T) is contoured from 61 vertical profiles. The salt-dominated density stratification is stable, with warmer, fresh water over cooler, saltier water. The velocity field is contoured from ≈360 profiles (5-min averages). The velocity data do not extend all the way to the bed due to interference of vertical acoustic side-lobe reflection with the ADCP.

[21] Maximum landward velocities in the pycnocline reach 1.25 m s^{-1} on the greater flood and 0.80 m s^{-1} on the lesser flood. Fluvial barotropic forcing partially balances the tidal barotropic forcing to reduce shear on flood. Maximum velocities differences across the entire water column are about 0.75 m s^{-1} on greater flood and about 0.50 m s^{-1} on lesser flood. Differences in σ_T reach about 15. The pycnocline rises further up into the water column and becomes thinner as the flood progresses. This suggests that during flood, local restratification of the water column associated with advection of the salt wedge dominates over mixing at the interface. On ebb, high shears and significant stratification exist at the interface. Velocity differences across the pycnocline on ebb are on the order of 2.0 m s^{-1}, and differences in σ_T reach about 15. A distinct feature is the sharp density interface on flood and a more diffuse interface on ebb. The separation of isopycnals on ebb can have two causes; interfacial mixing and/or differential advection of a longitudinal density gradient.

[22] The data reveal a strong correlation between the temperature and salinity in the estuary (Figure 4). The consistent linear dependence of temperature on salinity is indicative of the mixture of two distinct water masses. It also suggests that the turbulent diffusions of salt and temperature are the same ($K_S = K_T$), a point that is important to the use of the Osborn-Cox method.

4.2. Turbulence Analysis

4.2.1. Velocity Spectra

[23] Velocity spectra are used in the calculation of ϵ and Γ_0 and were calculated from measured time series of horizontal and vertical velocity components. Typical spectra of vertical and horizontal velocity during ebb mixing events are shown in Figure 5. The spectra during ebb mixing events have certain features in common: (1) the existence of a characteristic spectral shape (discussed below), (2) a region of isotropic turbulence as demonstrated by overlapping vertical and horizontal velocity spectra, and (3) a larger noise floor on horizontal velocity spectra than on the vertical velocity spectra. The enhanced signal near the low wavenumber end of the spectrum is the result of the combination of internal waves and frame motion.

[24] Fits to vertical spectra of turbulent velocity are used to determine ϵ, the dissipation rate of turbulent kinetic energy. The vertical velocity spectra were fit to a modified Kolmogorov spectrum for the inertial subrange. The modifications include (1) viscous as per *Pao* [1965]; (2) attenuation due to spatial averaging, and (3) contamination by instrument noise levels at high wavenumber. The dissipation rate, ϵ, is the variable parameter used to optimize the fit.

[25] Kolmogorov's theory states that at sufficiently high Reynolds number, the statistical properties of turbulence at high turbulent wavenumber (small scales) is independent of the low wavenumber (large scales) where production occurs. At length scales smaller than the scale of production, the only parameters that can affect the energy density at wave number k ($E(k)$) are the rate of energy dissipation ϵ and the kinematic viscosity ν. With this assumption, dimensional arguments lead to the expression for $E(k)$;

$$E(k) = \epsilon^{2/3} k^{-5/3} F\left(\frac{k}{k_s}\right) \tag{8}$$

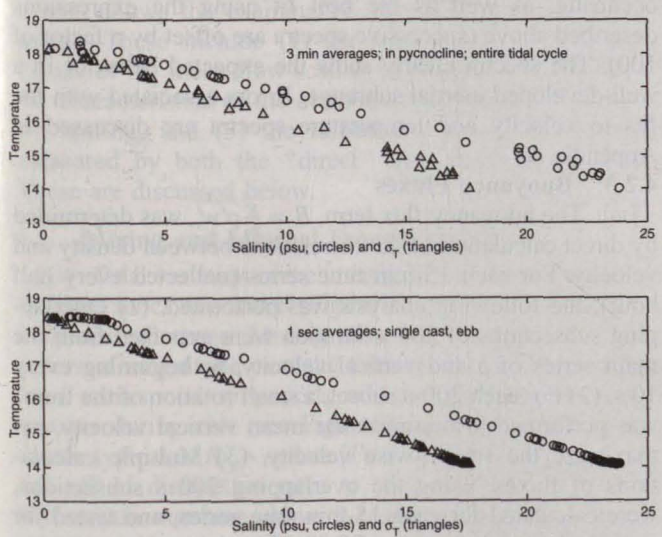

Figure 4. Temperature, salinity and σ_T relationships at experimental site. The top panel shows 3-min averages throughout the tidal cycle. The bottom panel shows an example of the simultaneous measurements taken during a single ebb cast.

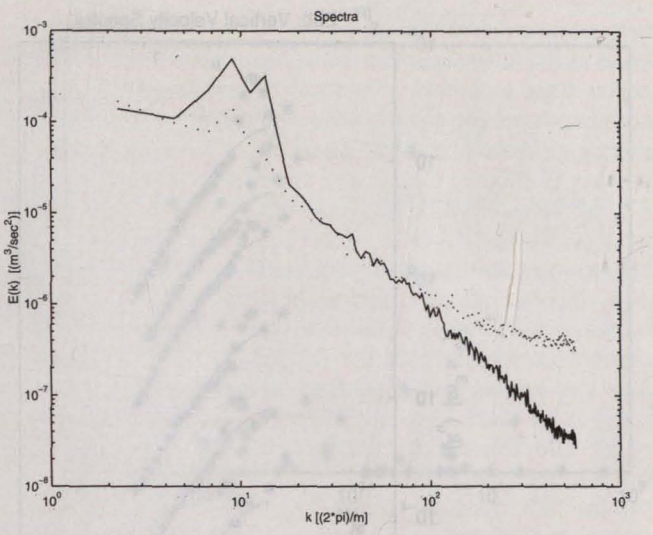

Figure 5. Typical velocity spectra during mixing events. Both vertical (solid) and along current horizontal (dotted) spectra are shown. Elevated values of the horizontal $E(k)$ for $k > \approx 10^2$ are caused by an instrumental noise floor. $E(k)$ peaks at $k \approx 10^1$ result from frame motion and internal wave activity.

where

$$k_s = \left(\frac{\epsilon}{\nu^3}\right)^{\frac{1}{4}} \tag{9}$$

where $k_s = LK^{-1}$ is the Kolmogorov wavenumber scale; i. e. the wavenumber at which viscosity becomes important in the dynamics. In the inertial subrange, where viscous effects are absent, the energy density $E(k)$ depends only on the wavenumber k, so $F\left(\frac{k}{k_s}\right)$ is constant.

[26] At higher wavenumbers, viscous effects are important, and $F\left(\frac{k}{k_s}\right)$ is not a constant. *Pao* [1965] asserted that the cascading rate, $\sigma(k) = \frac{\partial k}{\partial t}$ (the rate that an energy spectral element is transferred across k) is dependent on ϵ, the dissipation rate, and k, the wavenumber of the small eddies. Under these conditions, dimensional analysis leads to the Pao form of the spectrum [*Pao*, 1965], which, when combined with Kolmogorov's model for the inertial subrange, leads to an expression for the spectrum $E(k)$ that includes viscous effects,

$$E(k) = \alpha\epsilon^{2/3} k^{-5/3} \cdot \exp\left(-\frac{3}{2}\alpha\nu\epsilon^{-1/3} k^{4/3}\right). \tag{10}$$

[27] Equation (10) is applied and the spectra are derived numerically from an integral $\Phi_w(k_u)$ for the one-dimensional spectra [*George and Lumley*, 1973] while varying the parameter ϵ to obtain the best fit to the measured spectra.

$$\phi_w(k_u) = \frac{1}{2}\int_{-\infty}^{\infty}\int_{-\infty}^{\infty} \frac{E(k)}{4\pi k^4}\left(k^2 + k_u^2\right) W(k) dk_v dk_w + \sigma_{ww}^2 \tag{11}$$

where $W(k)$ is attenuation due to spatial averaging over the measuring volume and σ_{ww} is the noise floor.

[28] Measured variance and covariance are affected by the finite sensor volume of the ADV. *Voulgaris and Trowbridge* [1998] applied to the ADV a technique developed by

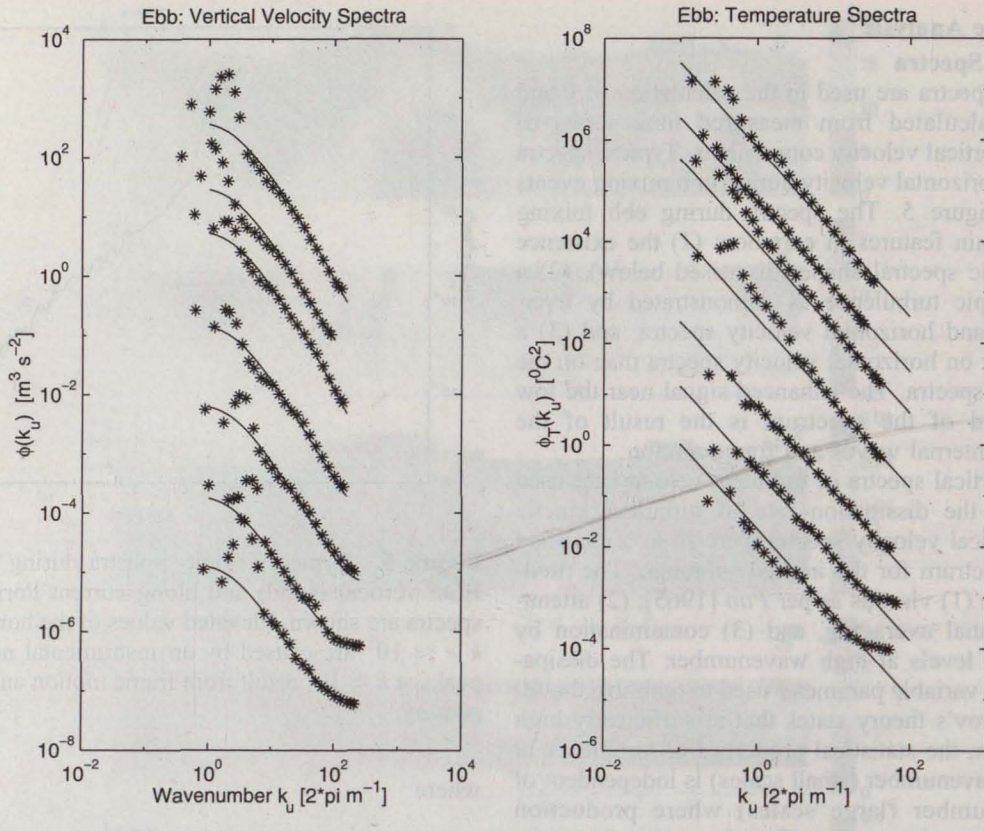

Figure 6. Spectra of vertical velocity, w', and temperature fluctuations, T', on ebb. Stars are measured spectra and lines are fits. Successive spectra are offset by a factor of 100. Good quality fits were possible for at least 1 decade, allowing reliable estimates of dissipation rates.

George and Lumley [1973] for the laser Doppler velocimeter (LDV) to account for this effect. They determined turbulent dissipation rates using spectral methods and compared them to theoretical rates using boundary layer theory. They found that the ADV measured velocity spectra are attenuated according to the transfer function proposed by *George and Lumley* [1973],

$$\frac{E(k)_{\text{measured}}}{E(k)_{\text{actual}}} = W(k) = \exp\left(-\frac{1}{4}\left(k_u^2 d_u^2 + k_v^2 d_v^2 + k_w^2 d_w^2\right)\right) \quad (12)$$

where (k_u, k_v, k_w) are the turbulent spectral wavenumbers and (d_u, d_v, d_w) are the sample volume dimensions along the (x, y, z) directions.

4.2.2. Temperature Spectra

[29] Spectra of temperature variance are used to estimate the potential energy dissipation rates from which Γ_d is determined. The theory of scalar dissipation predicts the existence of a convective subrange that has the same wavenumber dependence as that of velocity variance in the inertial subrange. In the region of nondissipative cascade of temperature variance the 1-D spectra have the form

$$\phi_s(k_u) = \beta \epsilon^{1/3} \chi_T k_u^{-5/3} \quad (13)$$

where χ_T is the temperature variance dissipation rate, and β is an empirically determined constant. The constant β has been determined by *Grant et al.* [1968] from measurements of temperature variance in turbulent flow. Again, use of this spectral form relies on the existence of a well-defined convective subrange, so that (equation (13)) can be fit to the temperature spectra. The quantity χ_T is used as a fitting parameter and ϵ is determined from the velocity spectra. Figure 6 shows vertical velocity and temperature spectra for a period when linear stability theory predicts mixing is occurring, as well as the best fit using the expressions described above (successive spectra are offset by a factor of 100). The spectra clearly show the expected behavior in a well-developed inertial subrange. Errors associated with the fits to velocity and temperature spectra are discussed in Appendix A.

4.2.3. Buoyancy Fluxes

[30] The buoyancy flux term, $B = \frac{g}{\rho_0}\overline{\rho' w'}$, was determined by direct calculation of the correlations between density and velocity. For each 15-min time series (collected every half hour), the following analysis was performed. (1) Overlapping subsections of 200-s duration were extracted from the main series of ρ and vertical velocity, w, beginning every 10 s. (2) For each 200-s subset, a small rotation of the frame was performed to minimize the mean vertical velocity and maximize the stream-wise velocity. (3) Multiple calculations of fluxes, using the overlapping 200 s subsections, were calculated for each 15-min time series, and tested for statistical significance, as described in Appendix A.

[31] With the coordinate system rotation performed, the calculated fluxes are perpendicular to the streamlines. If mean vertical velocities exist, the direction of the measured fluxes may differ slightly from the vertical. However, with 10 km as an estimate of the wedge length and 10 m as an

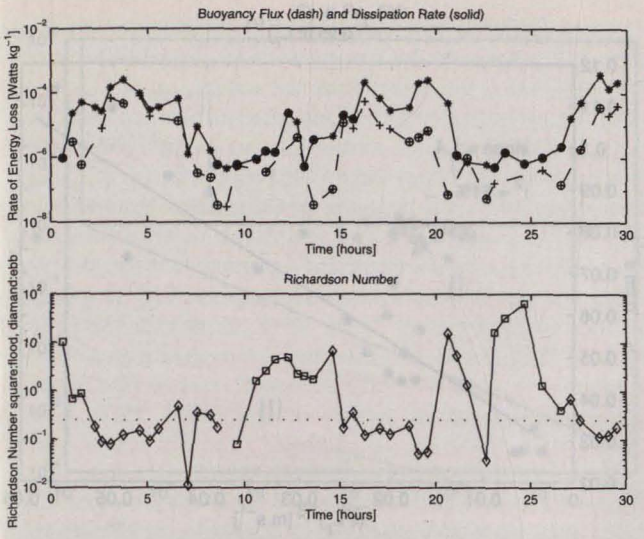

Figure 7. Measured B(+) and ϵ (*) at most half-hourly intervals of the 30-hour experiment. Both show a clear tidal signal. The measurements that have questionable statistical significance (in the case of B) or didn't pass the criterion $2L_R > L_{outer}$ (in the case of ϵ), are circled. Many of the data points below $\epsilon \approx 10^{-6}$ W kg^{-1} are at the background noise level of the measurements. The times series of gradient Richardson number, Ri_g, is also included to show the relationship between the turbulent and mean-flow characteristics.

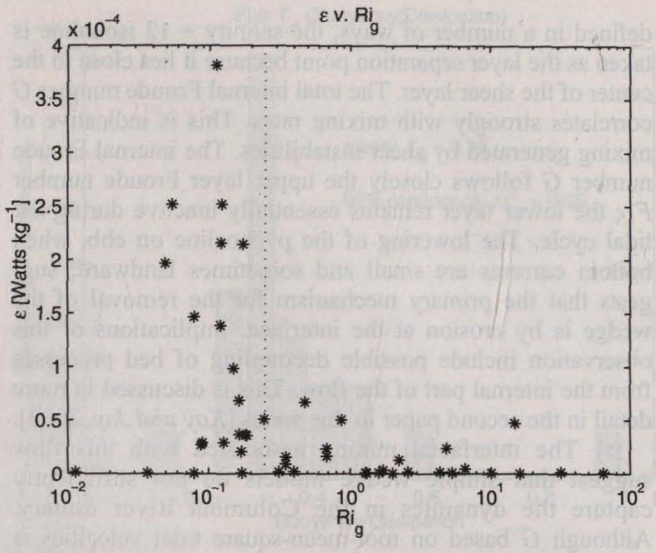

Figure 8. Measured dissipation rates as function of gradient Richardson number, Ri_g. Mixing is seen to become enhanced as Ri_g falls below 0.2–0.3. Ri_g rarely falls below about 0.1, not far from the critical value.

estimate of the change in height of the pycnocline, the ratio of horizontal to vertical velocities is $O(10^{-3})$, suggesting that the vertical velocities are very small. Therefore, the direction perpendicular to the streamlines differs from the true vertical by a few degrees at most.

5. Discussion

[32] The measurements of ϵ, χ_T and B during mixing events allows the examination of a number of important issues. These include (1) the relationship of mixing to values of the mean-flow scaling parameters R_{ig} and G, (2) the characteristics of the observed turbulence as suggested by scaling, and (3) the turbulent mixing efficiency as measured by both the "direct" and "indirect" methods. These are discussed below.

5.1. Mixing and Internal Froude Number

[33] Tidal variation in the interfacial mixing is apparent in the time series of ϵ and B (Figure 7), with $\epsilon > B$ as expected in almost all cases. Mixing rates vary by more than two orders of magnitude over the tidal cycle. The high mixing rates correspond to periods of low gradient Richardson number during ebb (see Figure 3). Although there exists scatter typical of Ri_g - ϵ plots [*Peters*, 1997], there is a clear fall off of dissipation rates to their background level at Richardson numbers above 0.2–0.3 (Figure 8). Scattered higher mixing rates at $Ri > 0.25$ may indicate of turbulence generated by shear instabilities [*Peters*, 1997], or mixing related to internal waves propagating from upstream topographic highs.

[34] The global current patterns generating the interfacial shear on ebb result primarily from tidal changes in surface slope and near-surface flow. The wedge below the pycnocline remains inactive during ebb. Figure 9 show the velocities and Froude numbers under the assumption of two-layer flow. Although the interfacial depth could be

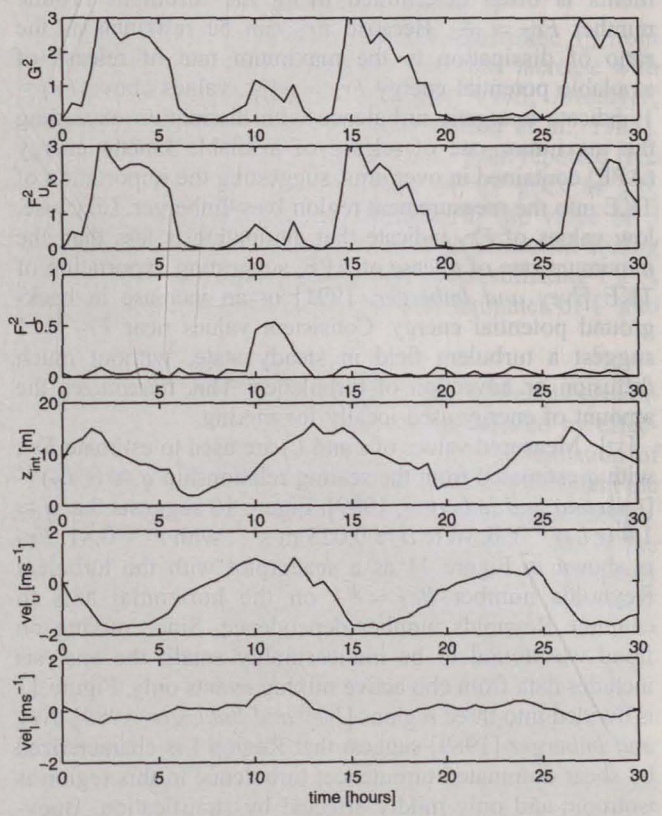

Figure 9. Total internal Froude number (G), upper layer (F_U) and lower layer (F_L) Froude numbers, interfacial depth (z_{int}), upper layer velocity (vel_u), and lower layer velocity (vel_l). The flow is supercritical on ebb, following upper layer Froude number. The lower layer is inactive throughout the tidal cycle.

defined in a number of ways, the salinity = 12 isohaline is taken as the layer separation point because it lies close to the center of the shear layer. The total internal Froude number G correlates strongly with mixing rates. This is indicative of mixing generated by shear instabilities. The internal Froude number G follows closely the upper layer Froude number F_U; the lower layer remains essentially inactive during the tidal cycle. The lowering of the pycnocline on ebb, when bottom currents are small and sometimes landward, suggests that the primary mechanism for the removal of the wedge is by erosion at the interface. Implications of this observation include possible decoupling of bed processes from the internal part of the flow. This is discussed in more detail in the second paper in this series [*Kay and Jay*, 2003].

[35] The interfacial mixing associated with this flow suggest that simple wedge models do not sufficiently capture the dynamics in the Columbia River estuary. Although G based on root-mean-square tidal velocities is subcritical, tidal variations cause the internal Froude number to go supercritical on ebb, when barotropic forces of the tide and river act in concert. The dynamics more closely resemble a forced shear flow than a gravity current. In the second part [*Kay and Jay*, 2003], we develop a model that allows an estimate of the momentum balance, mixing, and stress distribution during periods of active mixing.

5.2. Turbulence Characteristics

[36] The character of turbulence in laboratory experiments is often determined using the turbulent Froude number $Fr_T = \frac{q}{NL_T}$. Because Fr_T can be rewritten as the ratio of dissipation to the maximum rate of release of available potential energy $Fr_T = \frac{\epsilon}{N\,APE}$, values above $Fr_T = 1$ indicate energetic turbulence with dissipation exceeding the maximum rate of release of available kinetic energy (APE) contained in overturns, suggesting the importation of TKE into the measurement region Ivey-Imberger. Likewise, low values of Fr_T indicate that dissipation is less than the maximum rate of release of APE, suggesting exportation of TKE [*Ivey and Imberger*, 1991] or an increase in background potential energy. Consistent values near $Fr_T \approx 1$ suggest a turbulent field in steady state, without much diffusion or advection of turbulence. This maximizes the amount of energy used locally for mixing.

[37] Measured values of ϵ and L_T are used to estimate Fr_T with q estimated from the scaling relationship $q \cong (\epsilon\, L_T)^{1/3}$ [*Luketina and Imberger*, 1989]. Figure 10 suggests that $q \approx 1.4\,(\epsilon\, L_T)^{1/3} + \mathrm{b}$, were $b \approx 0.025$ m s^{-1}, with $r^2 = 0.81$. Fr_T is shown in Figure 11 as a scatterplot with the turbulent Reynolds number $Re_T = \frac{qL_T}{\nu}$ on the horizontal axis to examine Reynolds number dependence. Since mixing on flood was found to be immeasurably small, the analysis includes data from ebb active mixing events only. Figure 11 is divided into three regions [*Ivey and Imberger*, 1989]. *Ivey and Imberger* [1989] suggest that Region I is characterized by shear dominated turbulence; turbulence in this region is isotropic and only mildly affected by stratification. Buoyancy starts to significantly affect the flow in region II where turbulence becomes anisotropic at larger scales and internal waves begin to appear. In region III, all fluctuations are wave-like and buoyancy fluxes fall to zero.

[38] The consistent aggregation of the points around $Fr_T \leq 1$ suggests the existence of a combined turbulence-internal wave field. This is consistent with evidence of measurable mixing at gradient Richardson number $Ri_g > 0.25$, resulting from local shears associated with internal wave exceeding background levels. In this regime, the measured overturn scales match the maximum overturn scale as determined by ϵ, and mixing efficiency Γ is at its maximum value [*Ivey and Imberger*, 1989].

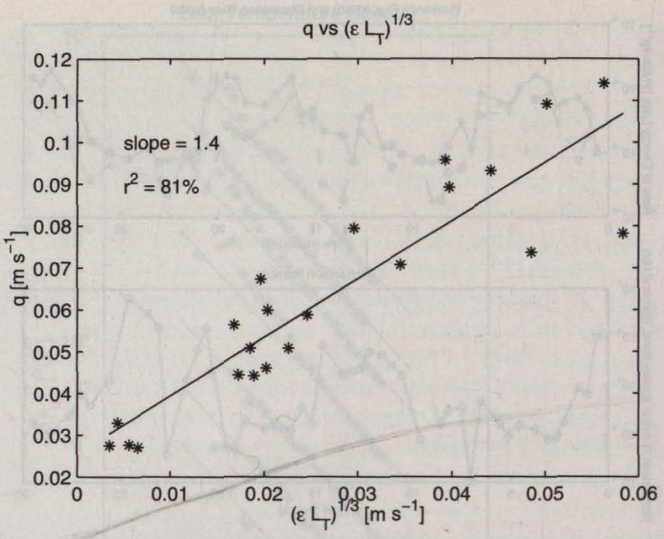

Figure 10. Scaling resulting from the assumption that the energy of eddies is dissipated in one overturn, $q = (\epsilon L_T)^{1/3}$. The plot shows good correspondence, with a slope of about 1.4.

5.3. Mixing Efficiency Γ

[39] Data that pass both the significance test for B and the length scale test for ϵ (see Appendix A) are used to estimate the mixing efficiency. Γ_0 was calculated for each of the 200-s subsections and all data are included in a single histogram of $log_{10}(\Gamma_0)$ (Figure 12). The mean and 95% confidence interval in Γ_0 are calculated by fitting the histogram to a normal distribution (Figure 12). The geometric mean is calculated from the fit to be $\mu_g = -0.65$. Γ_0 and its 95% confidence limits are then taken to be $\Gamma_0 = 10^{\mu_g \pm 1.96\sigma_g n^{-1/2}}$ which has an ensemble average of $\Gamma_0 = 0.22 \pm 0.03$ ($R_f = 0.18 \pm 0.02$) where σ_g is the standard deviation of the geometric mean. Dissipation scale quantities are expected to be lognormal. However, Γ_0 is a ratio of a production scale measurement to a dissipation scale measurement so the statistics of Γ_0 do not follow any tractable statistical form. Thus, following *Gargett and Moum* [1995], the decision to use the logarithm results from the large range of scales plotted rather than an expected statistical form. In order to check the sensitivity of the calculation of Γ_0 to the assumption of lognormality, the equivalent operations were performed on the distribution of $1/\Gamma_0$, and the 95% confidence limits in Γ_0 were calculated using $\Delta\Gamma_0 = (\Gamma_0)^2\Delta(1/\Gamma_0)$. Resulting Γ_0 and confidence limits were essentially unchanged. Figure 13 is a histogram of Γ_d. Fewer measurements were possible due to averaging needed for spectra. The mean of Γ_d is 0.36 and its 95% confidence interval is 0.06, corresponding to $R_f = 0.26 \pm 0.03$.

[40] There is a discrepancy in mixing efficiency as measured by the two methods, with $\Gamma_d > \Gamma_0$. There are

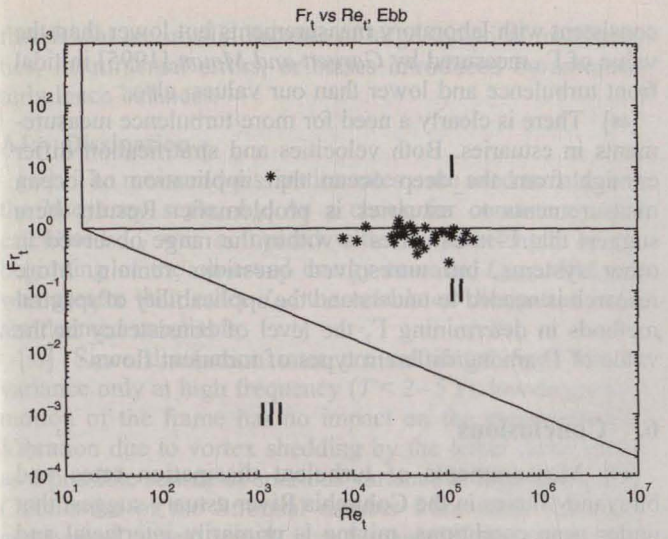

Figure 11. Measured turbulence characteristics plotted on an Fr_T vs. Re_T diagram. The regions identified by *Ivey and Imberger* [1991] are also shown.

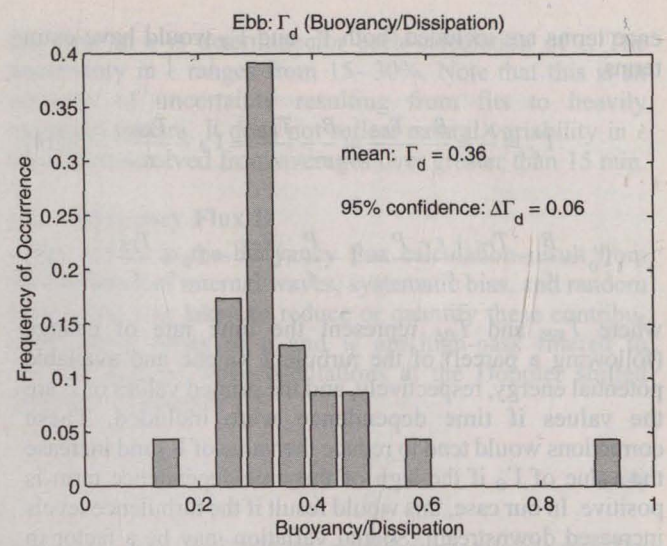

Figure 13. Histogram of Γ_d measured by calculating χ_{pe}/ϵ. The points used were determined to be from reliable spectral fits, based on the length scale test described in the text. Fewer determinations were possible due to the necessary averaging for spectra. The mean was calculated to be 0.36 and the 95% confidence interval is 0.06.

several factors that may contribute to the different values. These are described in the following subsections.

5.3.1. Validity of Spectrum

[41] Experimental evidence of the universal form of scalar spectra in the inertial-convective subrange is more scattered than that for the velocity spectral measurements [*Gargett*, 1985]. This has resulted in considerable uncertainty of the applicability of scaling based on equation (13). Furthermore, *Gargett* [1985] argues that the numerous observations of the $k^{5/3}$ form are likely associated with anisotropy in the turbulent field. If this is the case, the validity of any measurement using the inertial subrange scaling is brought into question. However, examination of spectra suggests that for the energetic events used to measure Γ, the turbulent field is isotropic in the inertial subrange. For the sake of our estimate, it is assumed that the form of the spectrum in equation (13) is applicable.

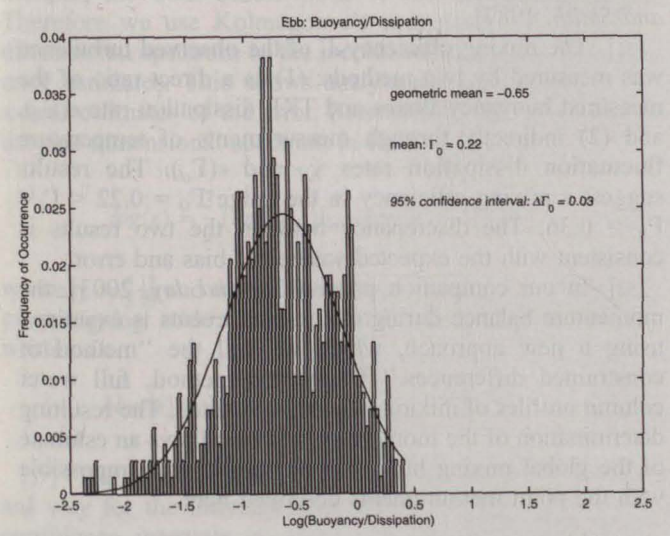

Figure 12. Histogram of Γ_0 measured by calculating B/ϵ. The points used were determined to be statistically significant. The mean was calculated by fitting a lognormal distribution. The ensemble average Γ_0 is 0.22 and 95% confidence interval is 0.03.

5.3.2. Value of the Empirical Constant β

[42] The empirical constant β used to determine χ_T from our spectra is not well established, and may increase with increasing Reynolds number [*Gargett*, 1985; *Mestayer*, 1982]. We employ a value β = 0.31 [*Grant et al.*, 1968]. However, values of β of up to ≈0.5 have been reported [see *Gargett*, 1985]. Since out estimate of χ_T goes as 1/β, doubling β will halve the χ_T estimate. If the value of β used here is too low, this would lead to an estimated mixing efficiency that is systematically high, overestimating Γ_d. A value of β = 0.5 would bring our two estimates of Γ into agreement.

5.3.3. Frame Motion

[43] Slight vertical motion of the frame as well as systematic errors tend to cause B to be underestimated by effectively high-pass filtering the data. Thus a combination of systematic error and bias in estimates of B might explain the discrepancy between Γ_0 and Γ_d if both were large enough. Systematic error in B could account for about 20% of the discrepancy. It is unlikely, however, that low-frequency frame motion can account for about 80% of the difference, given that the flux-containing eddies are rarely bigger than the frame. Random motion of the frame at higher frequencies have random phase and were removed by averaging.

5.3.4. Ignored Terms in the Turbulent Kinetic and Potential Energy Balances

[44] It is possible that the forms of the balances assumed for the turbulent kinetic energy and the available potential are too simplistic. The TKE balance used, for example, retains the dissipation, production, and buoyancy terms, and discards the time-dependence, diffusion, and pressure-work terms. The potential energy balance retains only the production and dissipation terms, and discards the time-dependence, and high-order correlations. If the time-depend-

ence terms are included, both Γ_0 and Γ_d would have extra terms,

$$\Gamma_d' = \frac{\chi}{\epsilon} = \frac{B - T_{KE}}{\epsilon} = \frac{B}{\epsilon} - \frac{T_{KE}}{\epsilon} = \Gamma_d - \frac{T_{KE}}{\epsilon} \quad (14)$$

$$\Gamma_0' = \frac{B}{\epsilon} = \frac{T_{PE} + \epsilon - P}{\epsilon} = 1 - \frac{P}{\epsilon} + \frac{T_{PE}}{\epsilon} = \Gamma_0 + \frac{T_{PE}}{\epsilon} \quad (15)$$

where T_{KE} and T_{PE} represent the time rate of change (following a parcel) of the turbulent kinetic and available potential energy, respectively, and the primed values of Γ are the values if time dependence were included. These corrections would tend to reduce the value of Γ_d and increase the value of Γ_0 if the sign of the time-dependence term is positive. In our case, this would result if the turbulence levels increased downstream. Spatial variation may be a factor in our experiment. The interfacial shear due to outflow over an inactive wedge increases seaward as the upper layer thins. Mass conservation requires that the interfacial shear increases as the ratio of the total depth to the thickness of the upper layer, H/h_u. This suggests that interfacial mixing increases seaward [*Simpson*, 1982]. The effect of this is an overestimation of Γ_d and an underestimation of Γ_0. This is a plausible explanation for the discrepancy between Γ_0 and Γ_d.

5.3.5. Filtering

[45] Filtering of the time series to remove variance associated with stable internal waves (Appendix A) possibly removes some mixing energy at near-internal wave frequencies. Since there is no way of resolving this signal against the background internal wave field, it must be removed. This removal of mixing at low frequencies would tend to underestimate Γ_0.

[46] These various possible biases render conclusive determination of the reason for the differences between Γ_0 and Γ_d difficult. All of the above possible errors are of a sign consistent with the observed discrepancy. However, the systematic bias due to the value of the empirical constant β used in the spectral fits has the potential to have the largest bias, followed by the effect of time dependence on both Γ_0 and Γ_d. The conclusion from the above analysis is that Γ_d is likely an upper bound to the mixing efficiency, with $\Gamma_0 = 0.22 < \Gamma < \Gamma_d = 0.36$.

[47] Although there are numerous measurements of χ_T and ϵ in the ocean, simultaneous measurements of mixing efficiency using both the direct flux measurements and dissipation rate measurements are rare in the ocean, and to our knowledge nonexistent in estuaries. *Gargett and Moum* [1995] measured mixing rates using direct measurements of B, ϵ and χ and in deep tidal straits. Interestingly they found $\Gamma_0 > \Gamma_d$, with Γ_0 exceeding by about a factor of two those found in the laboratory experiments summarized by *Ivey and Imberger* [1991]. They suggest a number of possible reasons for this difference, including the possibility that the laboratory and deep ocean measurements are all done at low Reynolds number (order 10^2 or smaller), whereas their measurements were made at $Re \approx 10^7$. They propose that high Re flows are under tested and low Re results may not apply. Other measurements of mixing efficiency include that of *Oakey* [1982] in the upper ocean and *Britter* [1974] in the atmosphere. Both find Γ in the range $0.15 < \Gamma < 0.2$, consistent with laboratory measurements but lower than the value of Γ_0 measured by *Gargett and Moum* [1995] in tidal front turbulence and lower than our values, also.

[48] There is clearly a need for more turbulence measurements in estuaries. Both velocities and stratification differ enough from the deep ocean that application of ocean measurements to estuaries is problematic. Results here suggest that Γ in estuaries is within the range observed in other systems, but unresolved questions remain. More research is needed to understand the applicability of spectral methods in determining Γ, the level of consistency in the value of Γ among different types of turbulent flows.

6. Conclusions

[49] Measurements of turbulent dissipation rates and buoyancy fluxes in the Columbia River estuary suggest that under neap conditions, mixing is primarily interfacial and limited to ebb. This interfacial mixing is dominated by shear between an active surface layer and an inactive salt-wedge layer, as demonstrated by a supercritical internal Froude number on ebb. The observed lowering of the pycnocline during ebb is therefore dominated by erosion, a feature not included in simple wedge models. The time-dependent nature of the flow suggests that interfacial shear and mixing need to be explicitly included in the momentum balance during ebb mixing. We develop a method to do this in a companion paper [*Kay and Jay*, 2003] and apply it to ebb mixing events measured here.

[50] Characteristics of the measured estuarine interfacial turbulence were examined by measurement of the turbulent Froude number Fr_T, which represents the relative effect of shear and buoyancy on the turbulent field. During the ebb mixing events, measured Fr_T was found to be close to unity. This suggests the existence of a combined turbulence-internal wave field. This is consistent with evidence of measurable mixing at gradient Richardson number $Ri_g > 0.25$, resulting from local shears associated with internal waves which raises shear above background levels [*Geyer and Smith*, 1987].

[51] The mixing efficiency Γ of the observed turbulence was measured by two methods: (1) as a direct ratio of the measured buoyancy fluxes and TKE dissipation rate $\epsilon(\Gamma_0)$, and (2) indirectly through measurements of temperature fluctuation dissipation rates χ_T and $\epsilon(\Gamma_d)$. The results suggest a mixing efficiency in the range $\Gamma_0 = 0.22 < \Gamma < \Gamma_d = 0.36$. The discrepancy between the two results is consistent with the expected sources of bias and error.

[52] In our companion paper [*Kay and Jay*, 2003], the momentum balance during ebb mixing events is examined using a new approach, which we call the "method of constrained differences." Using this method, full water column profiles of mixing rates are estimated. The resulting determination of the momentum balance allows an estimate of the global mixing budget, something that is impossible with the point measurements described here.

Appendix A: Errors in Dissipation Rate and Buoyancy Flux Measurements

[53] It is important to the validity of the results presented here to exclude estimates of the dissipation ϵ and buoyancy

flux B that are invalid because of large statistical uncertainties, instrumental errors, or biases introduced by assumed turbulence balances.

A1. Dissipation ϵ

[54] The measured dissipation rates ϵ are used to calculate the buoyancy scale, L_R. As a check for consistency, the calculated L_R was compared with the wavelength of the beginning of the observed energy cascade, L_{outer}. If L_{outer} was greater than twice L_R, the calculated dissipation rates are deemed unreliable.

[55] Since dissipation rates are calculated from fits to variance only at high frequency ($T < 2-5$ s), low-frequency motion of the frame has no impact on the measurements. Vibration due to vortex shedding by the tether cable arises as a possible source of spurious variance at high frequency. Calculation of the Strouhal number from cable thickness and typical current speeds give frequencies that range from 15 to 25 Hz, above our Nyquist frequency of 12.5 Hz. In addition, spectra show no signs of being pulled up at high wavenumber due to such vortex shedding.

[56] The spectral estimates of turbulent dissipation rates derived from Kolmogorov's theory and fit to the inertial subrange/dissipation range have uncertainties associated with (1) the empirically determined Kolmogorov constant, (2) confidence levels in the calculation of the spectrum, and (3) subsequent errors in the fit. Calculation of the dissipation rate ϵ from vertical velocity spectra requires the use of the empirically determined constant α. The value of $\alpha = 1.7$ was found by *Pao* [1965] to be the best fit for data from tidal streams [*Grant et al.*, 1968] and in a round air jet [*Gibson*, 1963], but values of α have been found from $\alpha = 1.4$ to $\alpha = 1.8$. Taking these varied results into account, we use a value of 1.6 ± 0.2 for the purposes of estimating errors. The 95% confidence intervals in the spectra were used to determine uncertainty in the log intercept $log_{10}(\Phi_{ww}(k_u))|_{log^{10}(k^u)=0}$. Although we use fits to the Pao spectrum, which includes viscous roll-off at high wavenumber, the bulk of the fit is to the inertial subrange. Therefore we use Kolmogorov's expression for the one-dimensional spectrum in the inertial subrange only, for our error estimates. This allows analytically determined, consistent estimates of the error. Rearranging the logarithm of the one-dimensional spectrum in terms of ϵ gives

$$log(\epsilon) = \frac{3}{2}\left(log(\phi_{ww})|_{int} - log(\gamma) - log(\alpha)\right), \tag{A1}$$

where $\gamma = \frac{4}{3}\frac{18}{55}$ and the subscript "int" refers to the intercept on a log-log scale. Then the variation of $log(\epsilon)$ can be written as

$$\delta log(\epsilon) = \frac{3}{2}\sqrt{\left(\delta log(\phi_{ww})|_{int}\right)^2 + \left(\delta log(\alpha)\right)^2}. \tag{A2}$$

[57] The term $(\delta\ log(\phi_{ww})|_{int})^2$ is calculated in the standard way for the intercept of a line fit to data, using 95% confidence intervals on $log(\phi_{ww}(k))$ as the error in the energy of the fit points. Then, using the relation for variation of logs,

$$\delta(x) = \frac{1}{log(e)} x \delta log(x) \tag{A3}$$

the error in ϵ is determine for each calculation of ϵ. The uncertainty in ϵ ranges from 15–30%. Note that this is an estimate of uncertainty resulting from fits to heavily averaged spectra. It does not reflect natural variability in ϵ that is not resolved from averages over greater than 15 min.

A2. Buoyancy Flux B

[58] Errors in the buoyancy flux calculation result from the influence of internal waves, systematic bias, and random error. Care was taken to reduce or quantify these contributions. Time series of ρ and w are high-pass filtered to exclude internal wave oscillations at the Doppler shifted buoyancy frequency f',

$$f' = f\left(1 + \frac{u}{c}\right)^{-1} \tag{A4}$$

where $f = N/2\ \pi$ and u is the mean horizontal velocity. The internal wave speed is estimated as $c = \sqrt{g\frac{\Delta\rho_p}{\rho_0}h_p}$, where $\Delta\rho_p$ is the density difference across the pycnocline, and h_p is the mean height of the pycnocline off the bed. Although not exactly the long-wave speed in the presence of shear (where wave speed is reduced), this expression gives the most conservative (highest frequency) estimate. That is, it excludes all internal waves up to the highest possible internal wave oscillations which result from waves of buoyancy frequency N traveling in the direction of the current. The ρ time-series is detrended and $F = \overline{\rho' w'}$ is calculated. With these calculated fluxes a mean and a standard deviation are defined,

$$F_n = \frac{\sum_j F_{nj}}{N} \tag{A5}$$

$$\sigma_n = \left(\frac{\left[\sum_j \left(F_{nj} - F_n\right)^2\right]}{N-1}\right)^{1/2} \tag{A6}$$

where F_{nj} is the jth subsection used in the nth half hour, F_n the mean value of flux at the nth half hour, and N is the total number of subsections used in the average.

[59] Measured values of turbulent fluxes F_n are subject to systematic bias (resulting from exclusion of lower frequencies), and to random error (associated with finite data) [*Lenschow et al.*, 1994]. Assuming an exponential flux correlation function, *Lumley and Panofsky*, 1964] derive an expression for the systematic underestimation of fluxes as

$$\frac{F - < F(T) >}{F} = \frac{2}{x} - \frac{2}{x^2} + \frac{2}{e^x x^2} \tag{A7}$$

where F is the true flux and $\langle F(T)\rangle$ is the measured flux from finite data. The quantity $x = \frac{T}{\mathcal{T}_{wp}}$, T is the sample length, and $\mathcal{T}_{wp}$ is the integral timescale of the flux correlation function $R_w\rho(\tau) = \langle w(t)\rho(t+\tau)\rangle$.

$$\mathcal{T}_{wp} = \frac{1}{F}\int_0^\infty R_{wp}(\tau)d\tau. \tag{A8}$$

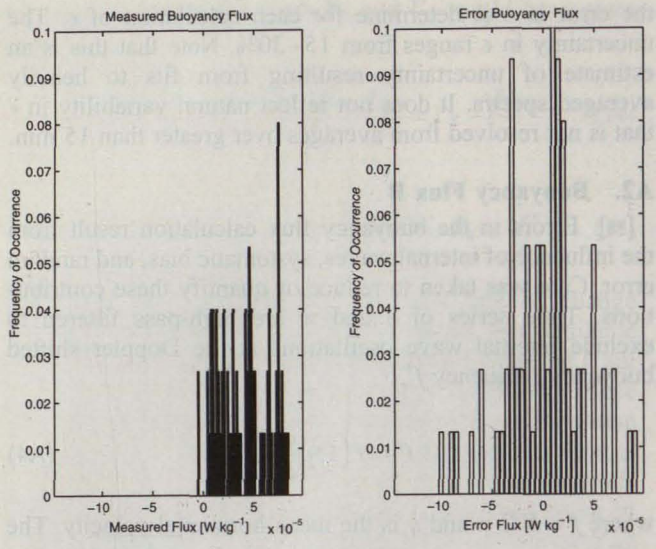

Figure 14. Distributions of measured buoyancy fluxes and error fluxes taken over one 15-min period. Error distributions are generated by multiplying together randomly selected time series of ρ' and w', and averaging. This example passed the test of statistical significance.

$\mathcal{T}_{wp}$ as estimated by the central width of $R_w\rho(\tau)$ reaches a maximum of about 20 s. Equation (A7) then predicts that fluxes are underestimated by a maximum of about 20%.

[60] Random error may be quite large, and estimates of random error suggest that a portion of the flux estimates are statistically indistinguishable from zero. Statistical significance is determined by applying a technique in which the distribution of calculated flux values in the ensemble is compared to a distribution function of "flux noise" values generated by taking the correlation of the flux components from different, randomly selected (and therefore independent) sections of the w' and ρ' time series [*Gargett and Moum*, 1995; *Yamazati and Osborn*, 1993]. This distribution function represents the flux noise associated with the data. Figure 14 provides an example of the distribution of the fluxes, F_{nj}, and a randomly generated distribution from independent sections of the time series. The criterion used to identify statistically significant fluxes is quite conservative, the 95% confidence interval of the flux estimate F_n not overlap 95% confidence level in the mean of the randomly generated distribution. The 95% confidence interval in F_n is calculated as

$$s_{Fn} = \pm 1.96 \frac{\sigma_n}{dof^{1/2}} \qquad \text{(A9)}$$

where *dof* is the number of degrees of freedom. The number of degrees of freedom should represent the number of flux carrying features passing the instrument in the time over which the flux is averaged. Measurements of the turbulence length scale suggest that flux carrying features can reach about 2 m in the vertical. During these mixing events, the integral timescale of the flux correlation function was found to reach 20 s with a typical velocity of 0.50 m s^{-1}. This suggests that eddies may have a 5:1 horizontal to vertical aspect ratio due to stretching. Therefore, we estimate *dof* as the number of features of 5 times the turbulent length scale ($5 \cdot L_T$) passing the instrument during the averaging period. Using this criterion, the majority of flux calculations on flood and around slack are found to be statistically insignificant. Most fluxes calculated on ebb were found to be significant. As an example (Figure 14), although the distributions overlap, the real distribution is found to be statistically distinguishable from the randomly generated distribution.

[61] **Acknowledgments.** This work was funded by the National Science Foundation grant OCE-9412928 (Columbia River Land-Margin Ecosystem Research Project; LMER), and the Office of Naval Research grant N00014-97-1-0012 (Circulation in Stratified Tidal Channels and Straits) and a related ONR AASERT, N00014-97-1-0625.

References

Britter, R. E., An experiment of turbulence in a density stratified fluids, Ph.D. thesis, Monash Univ., Clayton, Victoria, Australia, 1974.

Ellison, T. H., Turbulent transport of heat and momentum from an infinte rough plane, *J. Fluid Mech.*, *2*, 456, 1957.

Gargett, A. E., Evolution of scalar psectra with the decay of turbulence in a stratified fluid, *J. Fluid Mech.*, *159*, 379–407, 1985.

Gargett, A. E., Observing turbulence with a modified acoustic doppler current profiler, *J. Atmos. Oceanic Technol.*, *11*, 1592–1610, 1994.

Gargett, A. E., and J. N. Moum, Mixing efficiencies in turbulent tidal fronts: Results from direct and indirect measurements of density flux, *J. Phys. Oceanogr.*, *25*, 2583–2608, 1995.

George, W. K., and J. L. Lumley, The laser-doppler velocimeter and its application to the measurement of turbulence, *J. Fluid Mech.*, *60*, 321–362, 1973.

Geyer, W. R., The time dependent dynamics of a salt wedge, Ph.D. thesis, Univ. of Wash., Seattle, 1985.

Geyer, W. R., and J. D. Smith, Shear instability in a highly stratified estuary, *J. Phys. Oceanogr.*, *17*, 1668–1679, 1987.

Gibson, M. M., Spectra of turbulence in a round jet, *J. Fluid Mech.*, *15*, 161–173, 1963.

Grant, H. L., R. W. Stewart, and A. Moilliet, Turbulence spectra from a tidal channel, *J. Fluid Mech.*, *12*, 241–263, 1962.

Grant, H. L., B. A. Hughes, V. M. Vogel, and A. Moilliet, Spectrum of temperature fluctuations in turbulent flow, *J. Fluid Mech.*, *34*, 423–442, 1968.

Gregg, M. C., Diapycnal mixing in the thermocline: A review, *J. Geophys. Res.*, *92*, 5249–5286, 1987.

Helfrich, K. R., Time-dependent two-layer hydraulic exchange flows, *J. Phys. Oceanogr.*, *25*, 359–373, 1995.

Itsweire, E. C., and K. N. Helland, Spectra and energy transfer in stably stratified turbulence, *J. Fluid Mech.*, *207*, 419–452, 1989.

Ivey, G. N., and J. Imberger, On the nature of turbulence in a stratified fluid, 1, The energetics of mixing, *J. Phys. Oceanogr.*, *21*, 650–658, 1991.

Jay, D. A., and J. D. Musiak, Particle trapping in estuarine tidal flows, *J. Geophys. Res.*, *99*, 20,445–20,461, 1994.

Jay, D. A., and J. D. Smith, Residual circulation in shallow estuaries, 2, Weakly stratified and partially mixed, narrow estuaries, *J. Geophys. Res.*, *95*, 733–748, 1990.

Jirka, G. H., and M. Arita, Density currents or density wedges: Boundary-layer influence and control methods, *J. Fluid Mech.*, *177*, 187–206, 1987.

Kay, D. J., and D. A. Jay, Interfacial mixing in a highly stratified estuary, 2, A "method of constrained differences" approach for the determination of the momentum and mass balances and the energy of mixing, *J. Geophys. Res*, doi:10.1029/2000JC000253, in press, 2003.

Kraus, N. C., A. Lohrmann, and R. Cabrera, New acoustic meter for measuring 3-d laboratory flows, *J. Hydraul. Eng.*, *120*, 406–412, 1994.

Lenschow, D. H., J. Mann, and L. Kristensen, How long is long enough when measuring fluxes and other turbulence statistics, *J. Atmos. Oceanic Technol.*, *11*, 661–673, 1994.

Lohrmann, A., B. Hacket, and R. Cabrera, High resolution measurements of turbulence, velocity and stress using a pulse-to-pulse coherent sonar, *J. Atmos. Oceanic Technol.*, *7*, 19–37, 1990.

Lohrmann, A., R. Cabrera, and N. C. Kraus, Acoustic-doppler velocimeter (adv) for laboratory use, paper presented at Conference on Fundumentals and Advantages in Hydraulic Measurements and Experimentation, Am. Soc. of Civil Eng., Reston, Va., 1994.

Lu, Y., and R. G. Lueck, Using a broadband adcp in a tidal channel, II, Turbulence, *J. Atmos. Oceanic Technol.*, *16*, 1568–1579, 1999.

Luketina, D. A., and J. Imberger, Turbulence and entrainment in a buoyant surface plume, *J. Geophys. Res.*, *94*, 12,619–12,636, 1989.

Lumley, J., and H. Panofsky, The Structure of Atmospheric Turbulence, 239 pp., John Wiley, New York, 1964.

Mestayer, P., Local isotropy and anisotropy in a high-Reynolds-number turbulent boundary layer, *J. Fluid Mech.*, *125*, 475–503, 1982.

Oakey, N. S., Determination of the dissipation of turbulent kinetic energy from simultaneous temperature and velocity shear microstructure measurements, *J. Phys. Oceanogr.*, *12*, 256–257, 1982.

Osborn, T. R., Estimates of the local rate of vertical diffusion from dissipation measurements, *J. Phys. Oceanogr.*, *10*, 83–89, 1980.

Osborn, T. R., and C. S. Cox, Oceanic fine structure, *Geophys. Fluid Dyn.*, *3*, 321–345, 1972.

Ozmidov, R. V., On the turbulent exchange in a stably stratified ocean, *Izv. Acad. Sci. USSR Atmos. Oceanic Phys.*, *8*, 853, 1965.

Pao, Y., Structure of turbulent velocity and scalar fields at large wavenumbers, *Phys. Fluids*, *8*(6), 1063–1075, 1965.

Pedersen, F. B., Environmental Hydraulics: Stratified Flows, Springer-Verlag, New York, 1986.

Peters, H., Observations of stratified turbulent mixing in an estuary: Neap-to-spring variations during high river flow, *Estuarine Coastal Shelf Sci.*, *45*, 69–88, 1997.

Rattray, M., and E. Mitsuda, Theoretical analysis of conditions in a salt wedge, *Estuarine Coastal Mar. Sci.*, *2*, 375–394, 1974.

Sherwood, C. R., D. A. Jay, R. B. Harvey, P. Hamilton, and C. A. Simenstad, Historical changes in the columbia river, *Prog. Oceanogr.*, *25*, 271–297, 1990.

Simpson, J. E., Gravity currents in the laboratory, atmosphere, and ocean, *Ann. Rev. Fluid Mech.*, *14*, 213–234, 1982.

Stacey, M. T., S. G. Monismith, and J. R. Burau, Obsevations of turbulence in a partially stratified estuary, *J. Phys. Oceanogr.*, *29*, 1950–1970, 1999.

Stillinger, D. C., K. N. Helland, and C. W. V. Atta, Experiments on the transition of homogeneous turbulence to internal waves in a stratified fluid, *J. Fluid Mech.*, *131*, 91–122, 1983.

Voulgaris, G., and J. H. Trowbridge, Evaluation of the acoustic doppler velocimeter (adv) for turbulence measurements, *J. Atmos. Oceanic Technol.*, *15*, 272–289, 1998.

Yamazati, H., and T. Osborn, Direct estimates of heat flux in a seasonal thermocline, *J. Phys. Oceanogr.*, *23*, 503–516, 1993.

Zhu, Z., Exchange flow through a channel with an underwater sill, Ph.D. thesis, Univ. of B. C., Vancouver, Canada, 1996.

D. A. Jay, Department of Environmental Science and Engineering, Oregon Graduate Institute, Portland, OR 97291, USA. (djay@ccalmr.ogi.edu)

D. J. Kay, Geophysics 351650, University of Washington, Seattle, WA 98195, USA. (kay@geophys.washington.edu)